Available online at www.sciencedirect.com
SCIENCE DIRECT®
ELSEVIER
Physica D 184 (2003) 237–258
PHYSICA D
www.elsevier.com/locate/physd

Wave collapse in dispersive magnetohydrodynamics: direct simulations and envelope modeling

D. Laveder [a], T. Passot [a,*], C. Sulem [b], P.L. Sulem [a], D.S. Wang [c], X.P. Wang [d]

[a] *CNRS, Observatoire de la Côte d'Azur, BP 4229, 06304 Nice Cedex 4, France*
[b] *Department of Mathematics, University of Toronto, Toronto, Canada M5S 3G3*
[c] *Laboratory for Scientific and Engineering Computing, Academy of Science, Beijing, China*
[d] *Department of Mathematics, University of Science and Technology, Clear Water Bay, Kowloon, Hong Kong, PR China*

Abstract

An example of wave collapse arising in dispersive magnetohydrodynamics is analyzed by means of both direct numerical simulations and envelope formalism. It is shown that in spite of the presence of various types of waves and of purely hydrodynamic effects, the evolution of a longitudinally homogeneous Alfvén-wave beam propagating along an ambient magnetic field is accurately described by a cubic nonlinear Schrödinger equation with an external potential proportional to the initial wave intensity. In this description, an axisymmetric beam can only collapse on its axis when its transverse extension significantly exceeds the typical scale of the modulational instability of the carrying wave. An axisymmetric configuration is however unstable with respect to azimuthal perturbations, leading to off-center collapse, even in situations that are smooth when axisymmetry is preserved. In the case of a wave packet with a finite longitudinal extension, a minimum size is required for blowup, associated with the formation of strongly anisotropic magnetic structures.

PACS: 52.35.Bj; 52.35.Mw; 52.65.Kj

Keywords: Hall-magnetohydrodynamics; Alfvén waves; Wave collapse; Filamentation; Nonlinear Schrödinger equation

1. Introduction

It is well known that through a multiple-scale perturbation analysis, the evolution of a small-amplitude quasi-monochromatic dispersive wave can be described by envelope equations, such as the nonlinear Schrödinger (NLS) equation. In several dimensions, these equations can produce a finite-time blowup, called wave collapse [1], that can in fact cover different behaviors of the original system. As an example, the solutions of the multi-dimensional sine-Gordon equation remain smooth and the blowup of the associated NLS equation only reflects the breakdown of the modulation asymptotics, resulting from a local amplification of the original solutions [2]. In contrast, in the case of the self-focusing of a laser beam, the NLS singularity not only corresponds to a very strong local amplification of the wave intensity but also captures the global form of the emerging structures. In more complex systems, such

* Corresponding author.
E-mail address: passot@obs-nice.fr (T. Passot).

0167-2789/$ – see front matter © 2003 Elsevier B.V. All rights reserved.
doi:10.1016/S0167-2789(03)00223-9

as the magnetohydrodynamic waves in a plasma, it may be more delicate to figure out the characteristics of the physical phenomenon associated with the blowup of the solutions of the envelope equations. The dynamics of the physical system may indeed involve additional couplings that are filtered out when affecting scales different from those on which the asymptotics concentrates.

The aim of this paper is to analyze the predictive character of the envelope equations [3] governing the evolution of circularly-polarized Alfvén waves propagating along an ambient magnetic field. Such waves are of great interest both in natural and fusion plasmas, as the formation of small-scale structures may result in particle acceleration and heating of the medium. When their wavelength is not too large compared with the Larmor radius of the ions, the inertia of these particles is not negligible and the fluid description should retain the Hall effect that makes the Alfvén waves dispersive. Other sources of dispersion can originate from finite Larmor radius effects or from the presence of dust. We nevertheless concentrate on the Hall-magnetohydrodynamics (Hall-MHD), viewed as a paradigm for hydrodynamic systems involving dispersive waves. Comparisons are performed between direct numerical simulations of these equations and predictions of the envelope description. We mainly concentrate on collapse in planes transverse to the propagation, resulting in Alfvén-wave filamentation [4]. This phenomenon can be affected by the coupling to the magneto-sonic waves and also, in the case of waves of larger amplitude, by specific hydrodynamic processes. Filamentation of a weakly perturbed circularly-polarized plane Alfvén wave was confirmed by direct numerical simulations of the Hall-MHD equations [5]. Section 2 summarizes the main results of this study. The transverse dynamics of an Alfvén-wave beam with a uniform amplitude in the longitudinal direction is addressed in Section 3. In this case, the two-dimensional NLS equation governing the evolution of the Alfvén-wave amplitude also includes a repulsive potential proportional to the initial intensity of the wave. The properties of this system and the effect of enforcing the axisymmetry of the beam are discussed in Section 4. Three-dimensional wave packets are finally studied in Section 5 where the influence of their longitudinal extension on the occurrence of a wave collapse is analyzed. A brief conclusion is presented in Section 6.

2. Filamentation of Alfvén-wave trains

When the dissipative processes are neglected, the Hall-MHD equations with a pressure term identical to that of a polytropic gas, read

$$\partial_t \rho + \nabla \cdot (\rho \boldsymbol{u}) = 0, \tag{2.1}$$

$$\rho(\partial_t \boldsymbol{u} + \boldsymbol{u} \cdot \nabla \boldsymbol{u}) = -\frac{\beta}{\gamma} \nabla \rho^\gamma + (\nabla \times \boldsymbol{b}) \times \boldsymbol{b}, \tag{2.2}$$

$$\partial_t \boldsymbol{b} - \nabla \times (\boldsymbol{u} \times \boldsymbol{b}) = -\frac{1}{R_i} \nabla \times \left(\frac{1}{\rho} (\nabla \times \boldsymbol{b}) \times \boldsymbol{b} \right), \tag{2.3}$$

$$\nabla \cdot \boldsymbol{b} = 0. \tag{2.4}$$

As usual, ρ is the density of the plasma, $\boldsymbol{u}$ its velocity and $\boldsymbol{b}$ the magnetic field. The equations are here written in a non-dimensional form, choosing as velocity unit the Alfvén speed $c_\mathrm{A} = \mathcal{B}_0/\sqrt{4\pi\rho_0}$, where $\mathcal{B}_0$ is the magnitude of the ambient magnetic field and ρ_0 the mean density of the plasma. In addition, γ is the polytropic gas constant and $R_i = \Omega_i L/c_\mathrm{A}$ denotes the ratio of the length unit L to the ion inertial length c_A/Ω_i. It is also convenient to define the parameter $\beta = c_\mathrm{s}^2/c_\mathrm{A}^2$ (where c_s is the sound speed) that, up to a factor $\gamma/2$, measures the relative magnitude of the magnetic and thermal pressures.

Among the various waves governed by the Hall-MHD equations linearized about a uniform magnetic field, circularly-polarized monochromatic Alfvén waves propagating along the ambient magnetic field deserve a special

attention, since they are exact solutions of the Hall-MHD equations [6]. For an ambient field taken in the x-direction, they are defined by $b_y - \mathrm{i}\sigma b_z = -(\omega/k)(u_y - \mathrm{i}\sigma u_z) = B_0\,\mathrm{e}^{\mathrm{i}(kx-\omega t)}$, where $\sigma = +1$ or -1 depending on the right-hand (RH) or left-hand (LH) polarization, $\rho = 1$, $u_x = 0$ and $b_x = 1$. For forward propagation, the dispersion relation reads $\omega = (\sigma k^2/2R_i) + k\sqrt{1 + (k/2R_i)^2}$. It is noticeable that these ideal waves display some similarities with large-amplitude quasi-monochromatic circularly-polarized wave packets observed in the Earth or the Jupiter bow shock environment [7–9]. The linear instability of these waves and the forthcoming nonlinear evolution were addressed in [5,10] for small and moderate amplitudes, respectively.

The transverse or filamentation instability leading to the phenomenon of wave collapse is conveniently described in the context of envelope equations. Consider a quasi-monochromatic Alfvén wave with an amplitude of order $\epsilon \ll 1$, propagating along a unit ambient magnetic field. Its modulation is described in terms of the slow variables $X = \epsilon x$, $Y = \epsilon y$, $Z = \epsilon z$, $T = \epsilon t$, the field components being expanded as

$$
\begin{aligned}
&b_y = \epsilon b_{y_1} + \epsilon^2 b_{y_2} + \cdots, \qquad u_y = \epsilon u_{y_1} + \epsilon^2 u_{y_2} + \cdots, \qquad b_z = \epsilon b_{z_1} + \epsilon^2 b_{z_2} + \cdots,\\
&u_z = \epsilon u_{z_1} + \epsilon^2 u_{z_2} + \cdots, \qquad b_x = 1 + \epsilon^2 b_{x_2} + \epsilon^3 b_{x_3} + \cdots, \qquad u_x = \epsilon^2 u_{x_2} + \epsilon^3 u_{x_3} + \cdots,\\
&\rho = 1 + \epsilon^2 \rho_2 + \epsilon^3 \rho_3 + \cdots,
\end{aligned}
$$

where the prescribed magnitudes of the various field components select the Alfvén-wave eigenmode.

To leading order, monochromatic solutions are circularly-polarized and satisfy

$$b_1 = b_{y_1} - \mathrm{i}\sigma b_{z_1} = B\,\mathrm{e}^{\mathrm{i}(kx-\omega t)}, \tag{2.5}$$

$$u_1 = u_{y_1} - \mathrm{i}\sigma u_{z_1} = U\,\mathrm{e}^{\mathrm{i}(kx-\omega t)} \tag{2.6}$$

with $U = -(k/\omega)B$ and ω given by the Alfvén-wave dispersion relation.

At next order, one has

$$\rho_2 = \tilde{\rho}_2\,\mathrm{e}^{\mathrm{i}(kx-\omega t)} + \text{c.c.} + \bar{\rho}, \tag{2.7}$$

$$u_{x_2} = \tilde{u}_{x_2}\,\mathrm{e}^{\mathrm{i}(kx-\omega t)} + \text{c.c.} + \bar{u}, \tag{2.8}$$

$$b_{x_2} = \tilde{b}_{x_2}\,\mathrm{e}^{\mathrm{i}(kx-\omega t)} + \text{c.c.} + \bar{b}_x, \tag{2.9}$$

where overbars refer to non-oscillating contributions. The amplitudes of the oscillating parts are given by

$$\tilde{u}_{x_2} = \frac{\beta k}{\omega}\tilde{\rho}_2, \quad \tilde{\rho}_2 = -\frac{\mathrm{i}k}{2(\beta k^2 - \omega^2)}\partial_\perp^* B, \qquad \tilde{b}_{x_2} = \frac{\mathrm{i}}{2k}\partial_\perp^* B, \tag{2.10}$$

where $\partial_\perp^* = \partial_y + \mathrm{i}\sigma\partial_z$. The divergence that occurs for $\omega/k = \beta^{1/2}$ corresponds to the coincidence of the phase velocities of the Alfvén and magneto-sonic waves, a regime that is not amenable to the present formalism.

In a frame $\xi = X - v_\mathrm{g}T = \epsilon(x - v_\mathrm{g}t)$ moving at the group velocity $v_\mathrm{g} = \omega' = 2\omega^3/k(k^2 + \omega^2)$, the dynamics on the time scale $\tau = \epsilon T = \epsilon^2 t$ is governed by

$$\mathrm{i}\partial_\tau B + \frac{\omega''}{2}\partial_{\xi\xi} B + \alpha\Delta_\perp B - k v_\mathrm{g}\left(\frac{1}{v_\mathrm{g}}\bar{u}_x + \frac{k^2}{2\omega^2}\bar{b}_x - \frac{1}{2}\bar{\delta}\right)B = 0, \tag{2.11}$$

$$\epsilon\partial_\tau\bar{\delta} + \partial_\xi(\bar{u}_x - v_\mathrm{g}\bar{\delta}) = 0, \tag{2.12}$$

$$\epsilon\partial_\tau\bar{u}_x + \partial_\xi\left(\beta\bar{\delta} + \beta\bar{b}_x - v_\mathrm{g}\bar{u}_x + \frac{1}{2}|B|^2\right) = -\mathrm{i}\epsilon\frac{\alpha}{v_\mathrm{g}}(B\Delta_\perp B^* - B^*\Delta_\perp B), \tag{2.13}$$

$$(\epsilon\partial_\tau - v_\mathrm{g}\partial_\xi)^2\bar{b}_x - \partial_{\xi\xi}\bar{b}_x = \Delta_\perp\left(\beta\bar{\delta} + (\beta+1)\bar{b}_x + \frac{k^2}{2\omega^2}|B|^2\right), \tag{2.14}$$

where the dispersion and diffraction coefficients are given by $\omega'' = \mathrm{d}^2\omega/\mathrm{d}k^2$ and

$$\alpha = \frac{k\omega}{2(k^2+\omega^2)}\left(\frac{\omega^2}{k^3} - \frac{\beta k}{\beta k^2 - \omega^2}\right). \tag{2.15}$$

We also defined $\bar{\delta} = \bar{\rho} - \bar{b}_x$. Note that the right-hand side of Eq. (2.13) for the mean longitudinal velocity includes a higher-order corrective term that, together with the time-derivative contribution, becomes relevant in the limit of a quasi-transverse modulation. Retaining this term is crucial for capturing the filamentation instability [3]. It rewrites $(\epsilon/v_g)(\partial_\tau|B|^2 + \mathrm{i}(\omega''/2)(B\partial_{\xi\xi}B^* - \text{c.c.}))$, but since this correction is only relevant in the case of perturbations in the transverse or quasi-transverse directions, it can in fact be reduced to $(\epsilon/v_g)\partial_\tau|B|^2$.

2.1. Transverse perturbations

Eqs. (2.11)–(2.14) simplify in the special case of a purely transverse modulation. In this case, they are solved as

$$\bar{\delta} \equiv \bar{\rho} - \bar{b}_x = 0, \tag{2.16}$$

and

$$\bar{u}_x = \frac{1}{v_g}(|B|^2 - |B_0|^2). \tag{2.17}$$

Furthermore,

$$\epsilon^2\partial_\tau^2\bar{b}_x - (\beta+1)\Delta_\perp\bar{b}_x = \frac{k^2}{2\omega^2}\Delta_\perp|B|^2. \tag{2.18}$$

After a short transient compared with the time scale of the amplitude modulation, the mean longitudinal magnetic field perturbation reduces to[1]

$$\bar{b}_x = -\frac{k^2}{2(\beta+1)\omega^2}|B|^2. \tag{2.19}$$

In the case of an infinitely extended circularly-polarized plane Alfvén wave, the initial intensity $|B_0|^2$ reduces to a constant.

Up to a phase shift, one can get rid of this contribution in the potential of Eq. (2.11) which then reduces to the canonical two-dimensional NLS equation

$$\mathrm{i}\partial_\tau B + \alpha\Delta_\perp B - k\left(\frac{1}{v_g} - \frac{k^4 v_g}{4(\beta+1)\omega^4}\right)|B|^2 B = 0, \tag{2.20}$$

from which the criteria for a wave train to be modulationally unstable in the transverse directions (filamentation instability) are easily obtained [1,3].

2.2. Three-dimensional perturbations

2.2.1. Linear stability analysis

When dealing with fully three-dimensional perturbations, the complete system (2.11)–(2.14) has to be used. A detailed analysis of the linear instabilities affecting a circularly-polarized plane Alfvén wave is presented in [5]. For

[1] As in the case of the Zakharov equations for Langmuir waves [11], this adiabatic approximation for $\bar{b}_x = \bar{\rho}$ is expected to be broken very close to collapse and thus to affect the eventual asymptotic rate [12]. Here we do not address this regime that is far beyond the validity domain of the envelope formalism.

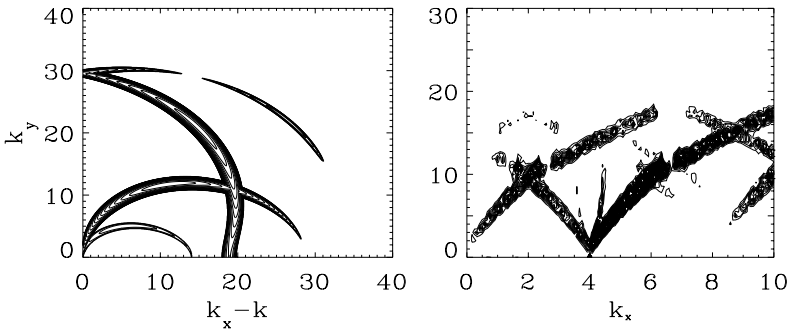

Fig. 1. Contours of the instability growth rate in wave vector space as obtained from the amplitude equations (2.11)–(2.14) (left) and unstable modes revealed by a direct simulation of the Hall-MHD equations (right) in the conditions described in Section 2.2.1, where the pump wavenumber is $k = 4$. In the left-hand side panel, the axes are labeled by the longitudinal and transverse wavenumbers of the modulation, expressed in the original variables.

the sake of simplicity, we concentrate here on the case of waves with left-hand polarization, where no longitudinal instabilities take place. As a specific example, we choose $\gamma = 2$, $\beta = 1.5$ and $R_i = 4$, with a pump wave characterized by a wavenumber $k = 4$ and an amplitude 0.1 in the physical units. For these parameters, Eq. (2.20) indicates that a plane wave is transversally unstable. Fig. 1 (left) that displays the contours of the instability growth rate in wave vector space, as analytically derived from the amplitude equations, shows that oblique and transverse instabilities coexist, the latter initiating the filamentation phenomenon. These oblique instabilities also exist in the framework of the Hall-MHD equations, as illustrated in Fig. 1 (right) resulting from a direct simulation using a Fourier pseudo-spectral code performed with the same parameters as those retained for the amplitude equations. Since the stability problem of the Hall-MHD equations consists in the perturbation of a periodic solution, the eigenmodes involve an infinite number of harmonics, leading to the periodically repeated pattern observed on the figure. In both descriptions, the instabilities are arrested at small scales, much beyond the range of validity of the envelope formalism. The very limited extension of this domain also explains that the similarity between the two panels of Fig. 1 is only qualitative.

2.2.2. The filamentation regime

Due to numerical constraints, both the direct simulations and the integrations of the amplitude equations presented in this paper involve a spectral truncation that cannot resolve the stabilization that occurs at small scales. In the context of the envelope equations, the small-scale oblique instabilities are strong enough to produce a rapid blowup of the simulations in the nonlinear regime. This contrasts with the direct simulations of the Hall-MHD equations where the large-scale dynamics develops before the small-scale oblique unstable modes are significantly amplified. Various regimes are obtained in this case, depending on the number of pump wavelengths retained in the longitudinal direction of the computational box whose transverse extension equals 16 pump wavelengths. The case where this number is relatively small is illustrated in Fig. 2, that corresponds to an initial Alfvén pump of amplitude $b_0 = 0.05$ and wavenumber $k = 1$, with only four wavelengths retained in the computational box. As in the previous section, $R_i = 4$, $\gamma = 2$ and $\beta = 1.5$. A Fourier pseudo-spectral code with a resolution of 128^3 collocation points is used. The initial perturbation of the Alfvén pump wave is taken in the form of a weak random noise, of maximal amplitude 5×10^{-4}, affecting only the largest scales of the density field (the four smallest wavenumbers in each direction). In such conditions, the linearly unstable modes present in the simulation are mostly limited to the transverse ones. One observes in this case the emergence of cylindrical structures aligned with the ambient field, whose intensity grows and thickness decreases in time. This formation of intense magnetic filaments is usually referred to as Alfvén-wave

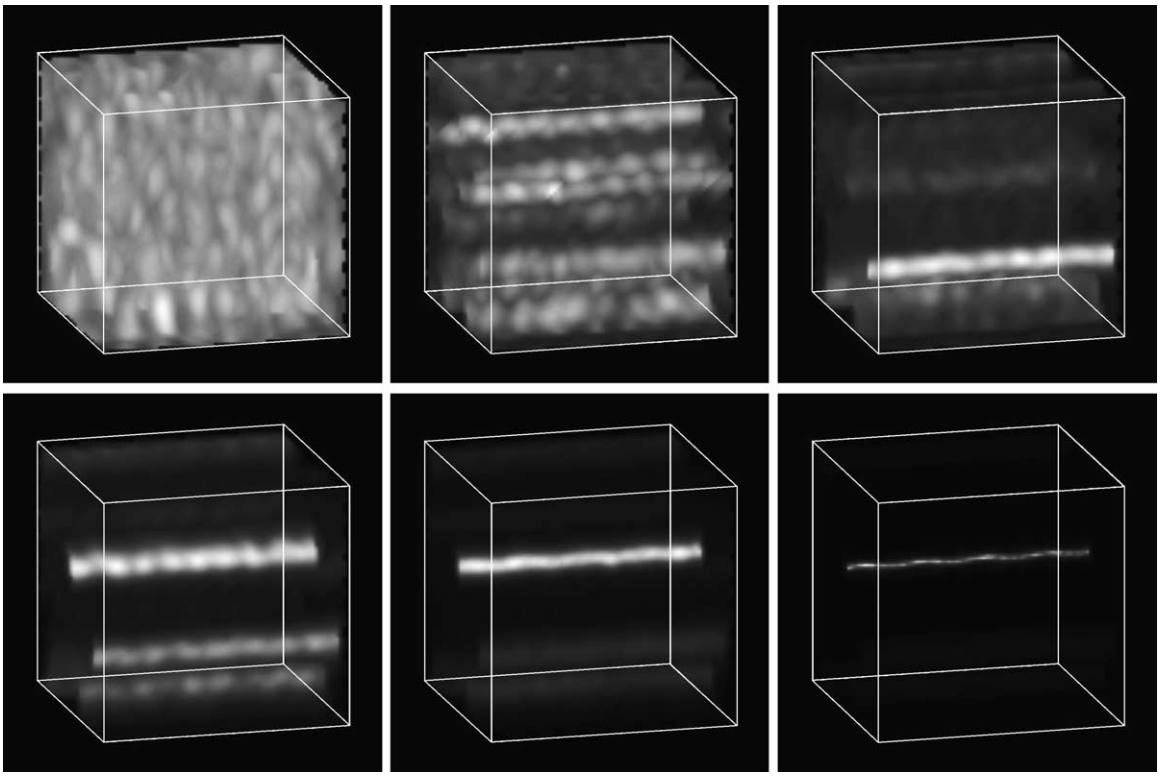

Fig. 2. Formation of intense magnetic filaments under the effect of the transverse modulational instability of a circularly-polarized monochromatic Alfvén wave with a wavelength equal to 1/4 of the longitudinal extension of the computational box (see Section 2.2.2). From left to right and from top to bottom, the panels correspond to the transverse magnetic field intensity at times $t = 25$, 200, 350, 500, 575 and 665.

filamentation and is associated with a transverse collapse of the Alfvén pump. An amplification of the wave intensity $|\boldsymbol{b}_\perp|^2$ by a factor 120 is observed at a time $t = 665$, as seen in Fig. 3 that displays the transverse magnetic field intensity in a plane orthogonal to the propagation. Slightly beyond this time, the resolution becomes insufficient and the computation must be interrupted. The simulated evolution can be described by the NLS equation (2.20) that indeed predicts that filamentation is a slow process developing on a time scale of the order of the inverse square amplitude of the wave. Fig. 4a shows that the expression (2.17) for the mean longitudinal velocity is accurate at the early stage of the collapse. At later times (Fig. 4b), the scaling assumptions underlying the derivation of the envelope equations breaks down and a significant deviation becomes visible for the few data points associated with the largest values of the amplitude. Most of the points remain nevertheless close to the theoretical line and the linear correlation coefficient is equal to 0.9988. A similar dynamics is observed in the case of an initial Alfvén pump of amplitude $b_0 = 0.1$ and wavenumber $k = 4$ corresponding to the conditions of Fig. 1, but the collapse is in this case less violent [5]. A simulation of the possible saturation of the collapse would require the development of a code based on a mesh refinement algorithm.

2.2.3. *Effect of unstable oblique modes*

When the size of the computational box is increased in the longitudinal direction in order to include more pump wavelengths, unstable modes with wave vectors that are almost but not exactly transverse to the propagation are retained by the spectral discretization. Such a regime is illustrated in Fig. 5 in the case where 32 wavelengths are

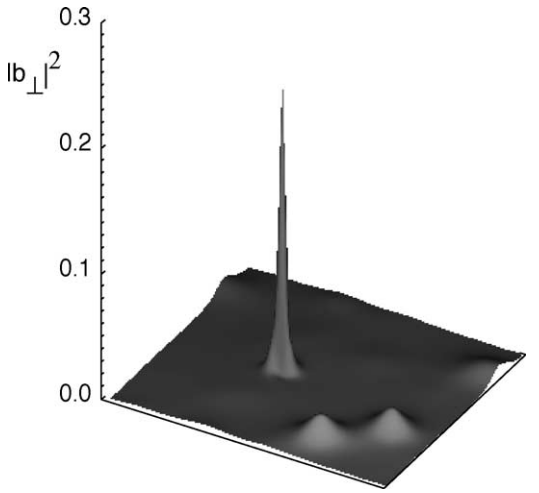

Fig. 3. Transverse magnetic field intensity $|\boldsymbol{b}_\perp|^2$ in a plane $x =$ const. transverse to the propagation in the conditions of the last panel of Fig. 2.

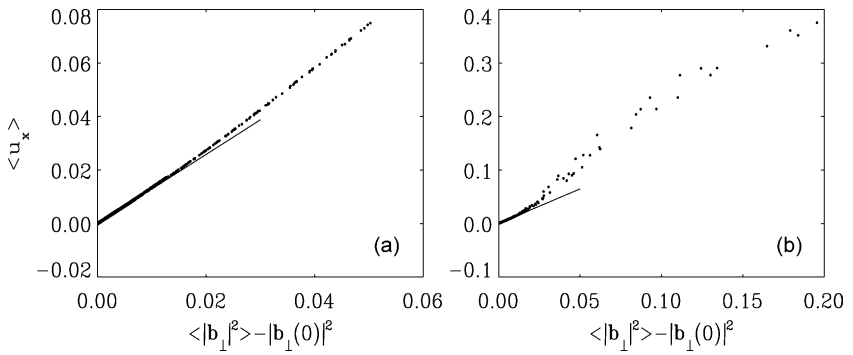

Fig. 4. Plot of the longitudinal velocity $\langle u_x \rangle$ versus the transverse magnetic field intensity $\langle |\boldsymbol{b}_\perp|^2 - |\boldsymbol{b}_\perp(0)|^2 \rangle$, averaged on the longitudinal direction at $t = 620$ (left) and 665 (right), in the conditions of Fig. 2. The straight line corresponds to Eq. (2.17) predicted by the envelope formalism for a purely transverse modulation.

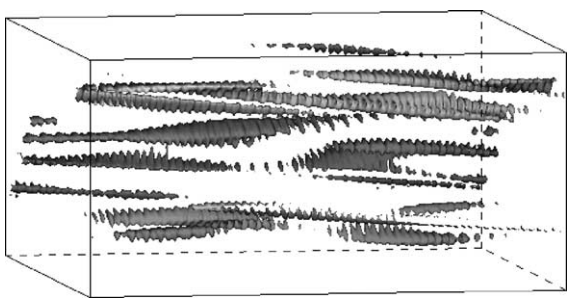

Fig. 5. Isosurface of the transverse magnetic field intensity at 1/3 of the maximum, at $t = 480$ for the simulation described in Section 2.2.3, when 32 wavelengths are included in the computational box.

retained, still keeping $b_0 = 0.05$ and $k = 1$. A resolution of 512×128^2 collocation points was used for this run. Magnetic structures elongated in the longitudinal direction are again formed, but make a well-defined angle with the propagation axis. Their intensity appears to be modulated and significantly weaker than in the previous computation. Furthermore the density fluctuations develop strong gradients associated with the steepening of magnetosonic waves [3]. Intermediate regimes displaying the progressive distortion of the magnetic filaments are discussed in [5].

3. Dynamics of an Alfvén-wave beam

3.1. Direct simulations of the Hall-MHD equations

A purely transverse dynamics can also develop in the case of an Alfvén-wave beam corresponding to a wave train whose amplitude rapidly decays in the transverse directions but remains constant along the propagation axis. In this case, the dynamics does not reduce to that described by the usual two-dimensional NLS equation. This situation is thus of special interest for comparison between direct simulations and predictions of the envelope equations. In particular, the possible formation of an intensity dip on the axis of the beam makes the collapse dynamics sensitive to the presence of azimuthal variations in the initial intensity.

The initial Alfvén-wave beam is produced by limiting the transverse extension of a circularly-polarized monochromatic Alfvén wave of amplitude $b_0 = 0.1$ and wavenumber $k = 4$ by means of a Gaussian envelope of the form $0.1\,\mathrm{e}^{-(1/288)[(y-10\pi)^2+\lambda^2(z-10\pi)^2]}$, where the factor λ, that measures departure from axisymmetry, is taken of order unity. The density and background magnetic field are initially equal to 1, while the initial longitudinal velocity is set to zero. We consider a periodic computational box whose transverse and longitudinal sizes are $L_\perp = 20\pi$ and $L_x = 24\pi$, respectively, in such a way that the finite-size effects remain negligible during the simulation times. A Fourier pseudo-spectral method is used for the space variables. The time stepping is made with a third order Runge–Kutta scheme [13].

We first discuss a simulation with a transverse anisotropy factor $\lambda = (1.5)^{1/2}$, performed with a resolution of 256^3 collocation points. Fig. 6 illustrates the evolution of the intensity of the magnetic field transverse to the propagation $|\boldsymbol{b}_\perp|^2$. A defocusing of the solution with no significant change in the form of the profile is first observed. An intensity dip then forms at the center of the structure producing a ring where the wave intensity continues to decrease for a while (reaching a minimum of 0.0077 at $t = 90$), before starting to increase. During this growth phase, the deviation from axisymmetry is strongly amplified, leading to the formation of intense peaks subject to a standard two-dimensional NLS collapse. Fig. 7 displays an isosurface of the transverse magnetic field intensity at a level equal to 1/3 of the maximum which reaches a value of $|B|^2 = 0.037$ at $t = 140$, just before the simulation breaks down. Note the presence of oscillations at the scale of the carrying Alfvén wave, associated with a weak departure from circular polarization. We anticipate that the further evolution will lead to the concentration of the transverse magnetic field intensity in thin filaments distant from the beam axis.

Another simulation was performed in similar conditions starting with an axisymmetric Alfvén-wave beam ($\lambda = 1$), using a resolution of 384×256^2 collocation points. The early dynamics appears similar to that of the previous run. Nevertheless, as seen in Fig. 8 (left), the amplification of the wave intensity is now delayed relatively to the non-axisymmetric case, even if the rates of growth appear comparable, at least as long as the simulations can be performed. The later behavior of the two runs could nevertheless be significantly different, as suggested by Fig. 8 (right) that compares the evolution of axisymmetric and non-axisymmetric beams in the context of the amplitude equations (2.11)–(2.14), where the simulation can be pushed far enough to see the saturation of the amplitude growth in the axisymmetric case. Furthermore, as for non-axisymmetric initial conditions, the circular

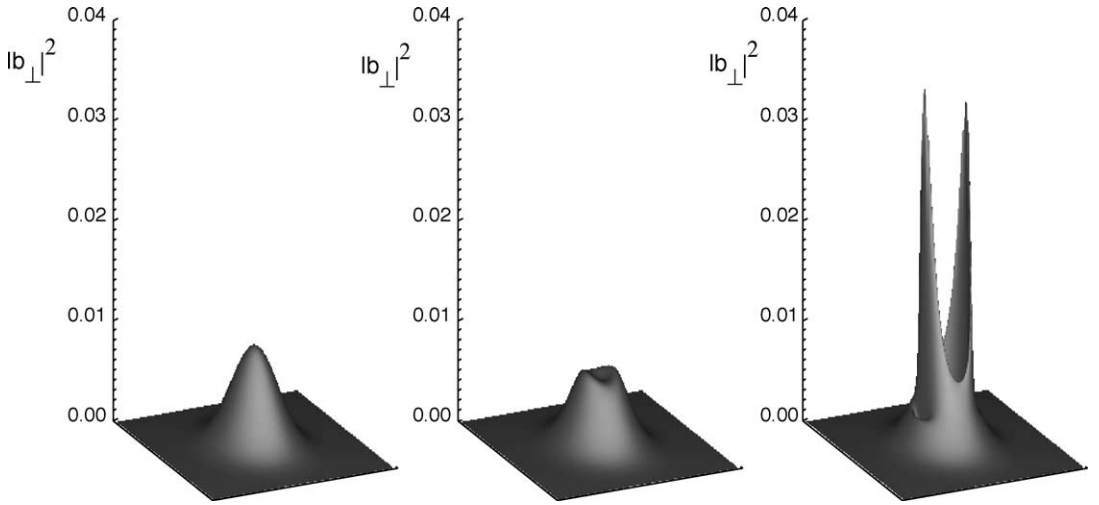

Fig. 6. Snapshots of the transverse wave intensity $|\boldsymbol{b}_\perp|^2$ in a transverse plane $x = \text{const.}$ at (from left to right) the initial time ($t = 0$), the instant of minimal intensity ($t = 90$) and the end of the simulation ($t = 140$), obtained by direct simulations of the Hall-MHD equations starting with an Alfvén-wave beam with a (transverse) amplitude profile $0.1\,\mathrm{e}^{-(1/288)[(y-10\pi)^2+1.5(z-10\pi)^2]}$.

polarization is weakly broken in the direct numerical simulation. As a consequence, a helical structure is visible when isolating the regions where the wave intensity is close to its maximum. Note that this effect is not reproduced by the envelope equations at the considered order. It is indeed subdominant on the time scale retained by the asymptotics.

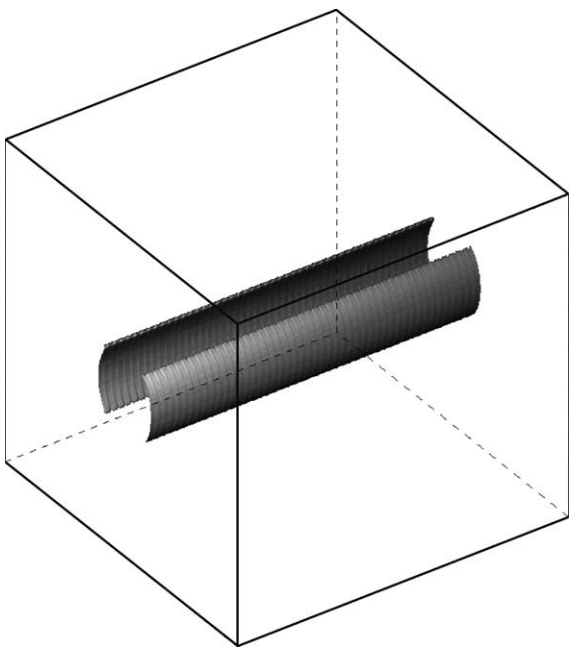

Fig. 7. Three-dimensional isosurface of the transverse magnetic field intensity at 1/3 of the maximum, corresponding to the rightmost panel in Fig. 6. The striation visible on the surface results from the polarization breaking.

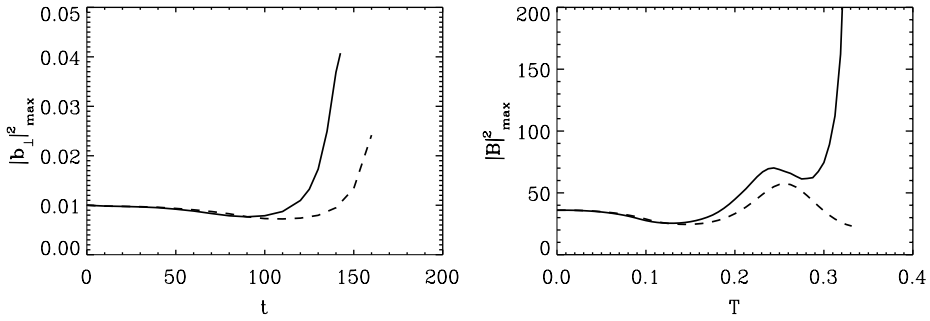

Fig. 8. Left: comparison of the evolution of the maximum intensity of an Alfvén beam in direct numerical simulations of the Hall-MHD equations for the non-axisymmetric ($\lambda = (1.5)^{1/2}$, solid line) and the axisymmetric ($\lambda = 1$, dashed line) initial conditions discussed in Section 3.1. Right: similar comparison in numerical integration of the envelope equations (2.11)–(2.14), for the non-axisymmetric initial condition $B_0 = 6\,\mathrm{e}^{-[1.3(y-\pi)^2+(z-\pi)^2]}$ (solid line) and the axisymmetric one $B_0 = 6\,\mathrm{e}^{-[(y-\pi)^2+(z-\pi)^2]}$ (dashed line) discussed in Section 3.2.

3.2. Integration of the envelope equations

Similar numerical computations were performed in the framework of the amplitude equations (2.11)–(2.14), using initial conditions $B_0 = 6\,\mathrm{e}^{-[1.3(y-\pi)^2+(z-\pi)^2]}$ and $B_0 = 6\,\mathrm{e}^{-[(y-\pi)^2+(z-\pi)^2]}$. The L^2-norm of both initial conditions significantly exceeds the critical value for collapse of the canonical two-dimensional NLS equation. As discussed in Section 2.1, in the absence of longitudinal modulation, this system reduces to a Zakharov system with an additional cubic term in the equation for the Alfvén-wave amplitude. The parameter ϵ is taken equal to 0.05. In both cases, the mean-field perturbations $\bar{\rho}$, $\bar{u}_x$ and $\bar{b}_x$ are initially zero. Compared with the direct simulations, these integrations benefit of both the elimination of the scale of the Alfvén-wave carrier and also of a purely two-dimensional character. The computations were done using a Fourier spectral method in a box of extension $L_\perp = 2\pi$ in both (transverse) directions. A resolution of 256×256 collocation points was used.

Snapshots of the intensity $|B|^2$ in a plane transverse to the propagation for the non-axisymmetric solution is displayed at a few typical times in Fig. 9. The time evolution of the maximum intensity corresponds to the solid line in Fig. 8 (right). A defocusing of the solution with no significant change in the form of the profile and a decay of the maximum wave intensity from 36 to about 28 at $T \approx 0.09$ is first obtained. A central dip then forms while the maximum intensity continues to decrease to about 24.5 at $T \approx 0.12$ and concentrates on a ring. Later on, after a further oscillation, the ring intensity increases (Fig. 9 (bottom left)) while the initial anisotropy is strongly amplified, leading to a concentration of the energy in very localized structures within the ring, suggesting NLS collapse in various points located at finite distance from the center. A maximum wave intensity of about 800 at $T = 0.325$ is obtained before the simulation breaks down.

With the axisymmetric initial conditions, the early dynamics is similar, as seen in Fig. 8 (right). The maximal intensity first decreases to about 25.5 around $T = 0.144$. The later on amplification of the ring intensity is however only a transient that proceeds to a time $T \approx 0.256$ where an intensity of 57.5 is obtained. A rapid defocusing then again takes place (see Fig. 10). The energy spreads to large distances and after a while the computation has to be interrupted due to the insufficient extension of the domain. No axisymmetry breaking is observed in this case, due to the low level of the numerical noise in spectral simulations, in contrast with the simulation based on an adaptive mesh algorithm discussed in Section 3.3.

A simulation with an intermediate degree of transverse non-axisymmetry for initial conditions of the form $B_0 = 6\,\mathrm{e}^{-[1.1(y-\pi)^2+(z-\pi)^2]}$ shows that the intensity on the ring formed at early times oscillates before developing a strong enough departure from axisymmetry to permit the formation of collapsing structures.

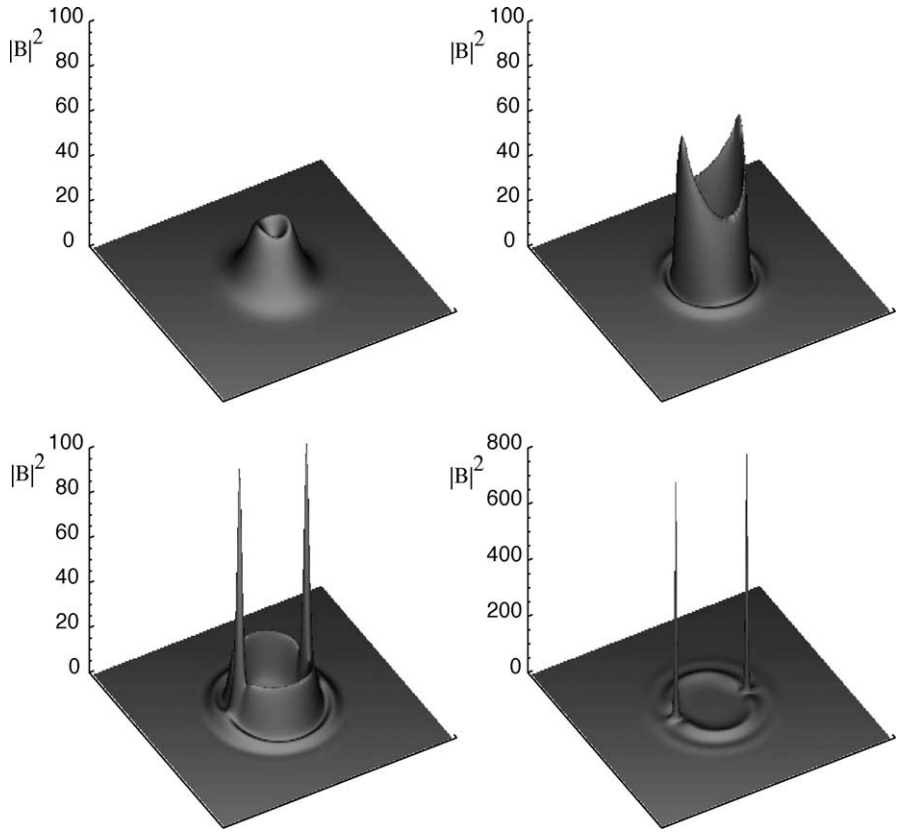

Fig. 9. Snapshots of the wave intensity $|B|^2$ in a transverse plane obtained by integration of amplitude equations (2.11)–(2.14), with initial conditions $B_0 = 6\,\mathrm{e}^{-[1.3(y-\pi)^2+(z-\pi)^2]}$. From left to right and top to bottom, the panels correspond to times $T = 0.125$, 0.244, 0.306 and 0.325.

Other integrations of the amplitude equations in regimes not amenable to direct simulations of the Hall-MHD equations were also performed. The regime where the radius of the Alfvén-wave beam is significantly larger than the wavelength of the linearly most unstable mode relatively to the modulational instability of a plane wave, is illustrated by considering an initial wave packet of amplitude $B_0 = 6\,\mathrm{e}^{-(1/100)[(y-10\pi)^2+(z-10\pi)^2]}$ in a simulation with 512×512 grid points. In this case, the system mostly behaves like a plane wave and is destabilized by the

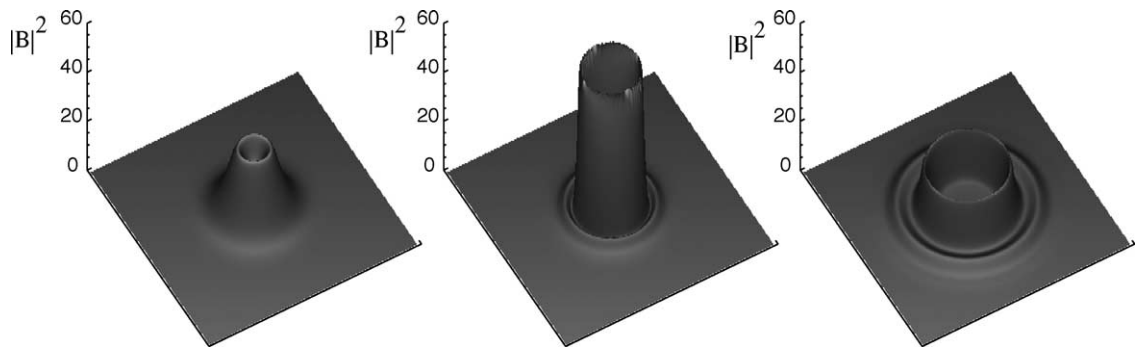

Fig. 10. Same as Fig. 9 for an axisymmetric initial beam $B_0 = 6\,\mathrm{e}^{-[(y-\pi)^2+(z-\pi)^2]}$ at times $T = 0.144$, 0.256 and 0.419.

truncation error that breaks the axisymmetry. Wave collapse then occurs. A similar conclusion holds when a weak non-axisymmetric perturbation is superimposed to the Gaussian profile. The axisymmetric solutions are indeed unstable. They nevertheless display interesting properties that are addressed in the next section.

3.3. The Schrödinger model

Due to the very localized character of the collapsing structures, only the early period of evolution during which the solution of the envelope equations is moderately amplified can be simulated using numerical codes with regularly distributed collocation points. This suggests to adopt a numerical algorithm based on an iterative grid redistribution (IGR) method [14] where the mesh sizes are dynamically adapted, depending on the local evolution. A description of the algorithm is presented in Appendix A. Furthermore, it may be convenient to use an even simpler envelope description by noticing that the longitudinal magnetic field $\bar{b}_x$, initially zero, relaxes to the expression (2.19) on a time scale much shorter than the typical time of the amplitude dynamics (Section 2.1). Eq. (2.11) then simplifies to a two-dimensional NLS equation:

$$\mathrm{i}B_t + \alpha\Delta_\perp B - k\left(\left(\frac{1}{v_\mathrm{g}} - \frac{v_\mathrm{g}k^4}{4(\beta+1)\omega^4}\right)|B|^2 - \frac{1}{v_\mathrm{g}}|B_0(\boldsymbol{x}_\perp)|^2\right)B = 0 \tag{3.1}$$

with an additional linear potential that now displays variations in the transverse directions and thus influences the Alfvén-wave dynamics. Its effect is equivalent to that of a localized inhomogeneity of the refractive index of the plasma near the axis of the beam. Note that this potential is repulsing, in contrast with the confining potentials arising in the description of Bose–Einstein condensation [15] or in the nucleation modeling in the Zakharov system [16].

It is convenient to rescale the space variables by a factor $|\alpha|^{1/2}$ (here α is negative) and the wave amplitude by a factor $g^{1/2}$ in the form $g^{1/2}B = \psi^*$, where $g = k((1/v_\mathrm{g}) - (v_\mathrm{g}k^4/4(\beta+1)\omega^4))$ and a star denotes the complex conjugate. It follows that $V = (k/gv_\mathrm{g})|\psi_0|^2$, where the subscript zero indicates the initial value. Eq. (3.1) then rewrites

$$\mathrm{i}\partial_t\psi + \Delta\psi + (|\psi|^2 - V(\boldsymbol{x}))\psi = 0 \tag{3.2}$$

with a potential $V(\boldsymbol{x})$ that is positive, bounded and rapidly decaying at infinity. This equation preserves the wave energy $\mathcal{E} = \int |\psi|^2\,\mathrm{d}\boldsymbol{x}$ and the Hamiltonian $\mathcal{H} = \int(|\nabla\psi|^2 - (1/2)|\psi|^4 + V|\psi|^2)\,\mathrm{d}\boldsymbol{x}$. In contrast, as a consequence of the breaking of the translation invariance, the linear momentum $\boldsymbol{P} = (\mathrm{d}/\mathrm{d}t)\int \boldsymbol{x}|\psi|^2\,\mathrm{d}\boldsymbol{x} = \mathrm{i}\int(\psi\nabla\psi^* - \psi^*\nabla\psi)\,\mathrm{d}\boldsymbol{x}$ is not conserved and obeys

$$\frac{\mathrm{d}\boldsymbol{P}}{\mathrm{d}t} = -2\int \nabla V|\psi|^2\,\mathrm{d}\boldsymbol{x}. \tag{3.3}$$

Furthermore, the "variance" $\mathcal{V} = \int |\boldsymbol{x}|^2|\psi|^2\,\mathrm{d}\boldsymbol{x}$ satisfies

$$\begin{aligned}\frac{\mathrm{d}^2\mathcal{V}}{\mathrm{d}t^2} &= \int(8|\nabla\psi|^2 - 4|\psi|^4 - 4\boldsymbol{x}\cdot\nabla V|\psi|^2)\,\mathrm{d}\boldsymbol{x} = 8\mathcal{H} - 8\int\left(V|\psi|^2 + \frac{1}{2}\boldsymbol{x}\cdot\nabla V|\psi|^2\right)\mathrm{d}\boldsymbol{x}\\ &= 8\mathcal{H} + 4\int V\boldsymbol{x}\cdot\nabla|\psi|^2\,\mathrm{d}\boldsymbol{x}.\end{aligned} \tag{3.4}$$

The right-hand side of (3.4) contains not only the Hamiltonian but also an additional term whose sign is not prescribed and strongly depends on the profile of the solution. This makes difficult to obtain simple conditions for collapse.

Note that, with the particular potential corresponding to the Alfvén-wave problem, the Hamiltonian reads

$$\mathcal{H} = \int \left(|\nabla \psi_0|^2 + \frac{1}{|\alpha|} \left(\frac{1}{1 - (v_g^2 k^4 / 4(\beta+1)\omega^4)} - \frac{1}{2} \right) |\psi_0|^4 \right) \mathrm{d}\boldsymbol{x}, \tag{3.5}$$

a quantity which is always positive.

The evolution predicted by Eq. (3.1) for an initial wave packet of amplitude $B_0 = 6\,\mathrm{e}^{-[1.3(y-\pi)^2+(z-\pi)^2]}$ is displayed in Fig. 11. The adaptive mesh computation is pushed up to $T = 0.3225$ when the maximum of $|B|^2$ reaches 1.4923×10^4. At this time the minimum mesh size is 1.2×10^{-3}. Such a simulation confirms the existence of the wave collapse suggested by the integration of the complete envelope equations.

A similar simulation is performed with the axisymmetric initial condition $B_0 = 6\,\mathrm{e}^{-[(y-\pi)^2+(z-\pi)^2]}$. It turns out that the axisymmetry of the solution is broken after a while by the numerical noise which is larger than in the spectral simulations. This effect enables the Alfvén wave to collapse in several spikes distributed on the intensity ring, which confirms the unstable character of the axisymmetric solutions in the present regime.

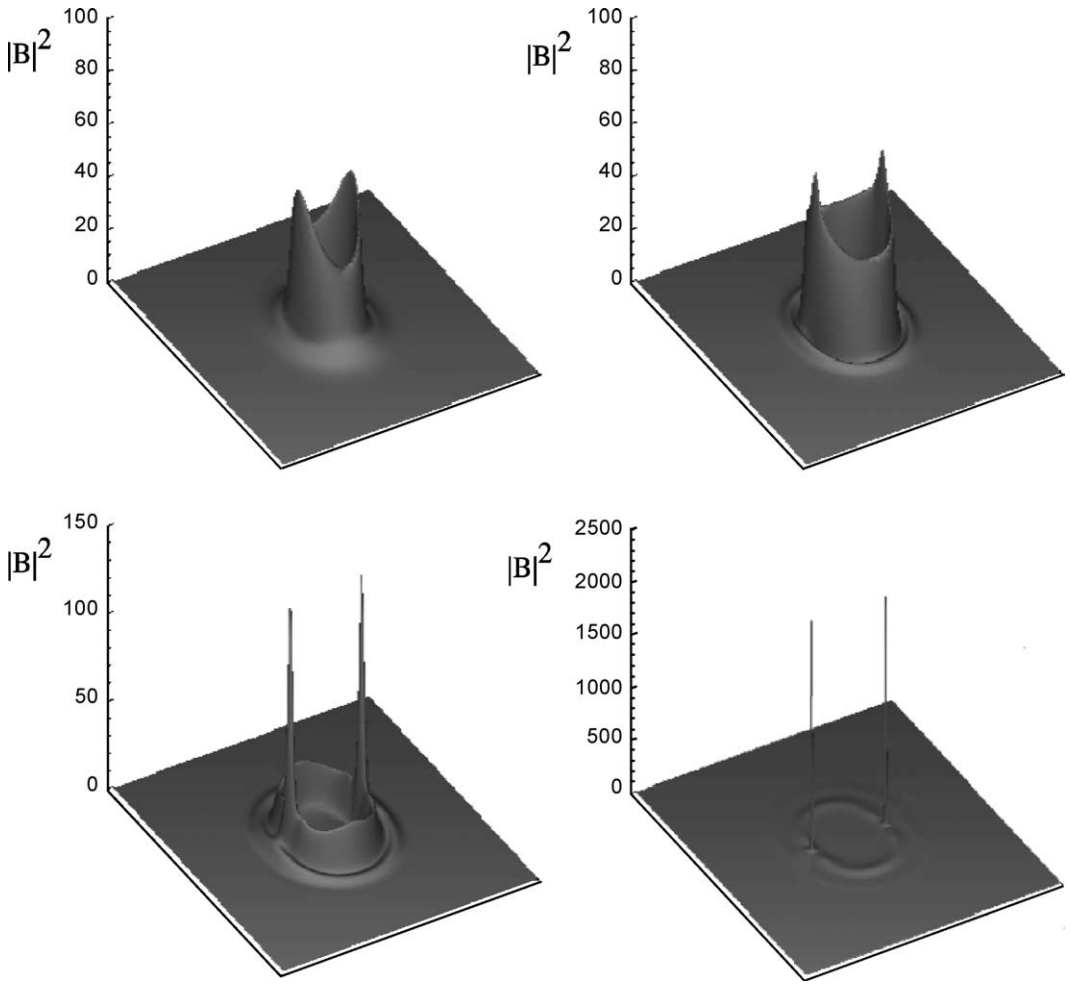

Fig. 11. Adaptive mesh integration of NLS equation (3.1) for an initial beam of amplitude $B_0 = 6\,\mathrm{e}^{-[1.3(y-\pi)^2+(z-\pi)^2]}$. From left to right and from top to bottom, the panels correspond to the wave amplitude $|B|^2$ at times $T = 0.211$, 0.268, 0.306 and 0.3216.

4. Dynamics of an axisymmetric beam

In spite of their unstable character, the axisymmetric solutions display interesting properties that are amenable to a more detailed analysis.

4.1. Rigorous results

The conservation laws enable one to show that an isotropic solution of (3.2) cannot collapse without blowing up at the origin. This property is a straightforward extension of Proposition 2 and Lemma 3 of Ref. [17] for the usual NLS equation, and results essentially from the observation that the external potential in Eq. (3.2) becomes irrelevant near collapse. More precisely, one has the following result.

Proposition 1. *If ψ is an isotropic solution of* Eq. (3.2) *which blows up at time T, then for all $a > 0$,*

(i) $$|\nabla\psi(t)|_{L^2(|\boldsymbol{x}|<a)} \to \infty \ \text{as} \ t \to T, \tag{4.1}$$

(ii) $$\limsup_{t\to T} \frac{|\psi|^4_{L^4(|\boldsymbol{x}|>a)}}{|\nabla(\rho_a\psi)|^2_{L^2}} = 0, \tag{4.2}$$

(iii) $$|\psi(t)|_{L^\infty(|\boldsymbol{x}|<a)} \to \infty \ \text{as} \ t \to T, \tag{4.3}$$

where ρ_a is a C^∞ radially symmetric scalar function such that $\rho_a(\boldsymbol{x}) = 1$ for $|\boldsymbol{x}| \le a$, and $\rho_a(\boldsymbol{x}) = 0$ for $|\boldsymbol{x}| > 2a$ with, for all $\boldsymbol{x}$, $\rho_a(\boldsymbol{x}) \le 1$.

The proof is based on two inequalities established in [17,18], respectively, and given for convenience in the lemma below in a form restricted to functions defined in $\mathbf{R}^2$.

Lemma 2. *Let v be a radially symmetric function in $H^1(\mathbf{R}^2)$. Then, for any $a > 0$:*

(i) $$|v|^2_{L^\infty(|\boldsymbol{x}|>a)} \le \frac{C}{a}|\nabla v|_{L^2(|\boldsymbol{x}|>a)}|v|_{L^2(|\boldsymbol{x}|>a)}, \tag{4.4}$$

(ii) $$|\rho_a u|^4_{L^4} \le C(|\nabla u|_{L^2(|\boldsymbol{x}|<2a)} + |u|_{L^2(|\boldsymbol{x}|<2a)})^2|u|^2_{L^2}, \tag{4.5}$$

where C denotes numerical constants.

Proof of Proposition 1.

(i) To establish (4.1), one writes

$$|\nabla\psi|^2_{L^2} \le \mathcal{H} + \frac{1}{2}\int |\psi|^4 \,\mathrm{d}\boldsymbol{x} + \int V|\psi|^2 \,\mathrm{d}\boldsymbol{x}, \tag{4.6}$$

$$|\nabla\psi|^2_{L^2} \le \mathcal{H} + C\mathcal{E} + \frac{1}{2}\int_{|\boldsymbol{x}|<a/2} |\psi|^4 \,\mathrm{d}\boldsymbol{x} + \frac{1}{2}\int_{|\boldsymbol{x}|>a/2} |\psi|^4 \,\mathrm{d}\boldsymbol{x}, \tag{4.7}$$

$$|\nabla\psi|^2_{L^2} \le \mathcal{H} + C\mathcal{E} + \frac{1}{2}|\rho_{a/2}\psi|^4_{L^4} + \frac{1}{2}\int_{|\boldsymbol{x}|>a/2} |\psi|^4 \,\mathrm{d}\boldsymbol{x}, \tag{4.8}$$

where C is a constant depending on the potential V. Using Eq. (4.5), one gets

$$|\nabla\psi|^2_{L^2} \le K + K_1(|\nabla\psi|_{L^2(|\boldsymbol{x}|<a)} + K_2)^2 + \frac{1}{2}\int_{|\boldsymbol{x}|>a/2} |\psi|^4 \,\mathrm{d}\boldsymbol{x}, \tag{4.9}$$

and by Eq. (4.4),

$$|\nabla\psi|^2_{L^2} \leq K + K_1(|\nabla\psi|_{L^2(|\boldsymbol{x}|<a)} + K_2)^2 + K_3|\nabla\psi|_{L^2}, \tag{4.10}$$

$$|\nabla\psi|^2_{L^2} \leq K + K_1(|\nabla\psi|_{L^2(|\boldsymbol{x}|<a)} + K_2)^2 + \tfrac{1}{2}|\nabla\psi|^2_{L^2} + K_4, \tag{4.11}$$

or

$$\tfrac{1}{2}|\nabla\psi|^2_{L^2} \leq K + K_1(|\nabla\psi|_{L^2(|\boldsymbol{x}|<a)} + K_2)^2 + K_4, \tag{4.12}$$

where the constants K_i's depend on the initial conditions and on the parameter a. It follows that if $|\nabla\psi|^2_{L^2} \to \infty$ as $t \to T$, so does $|\nabla\psi|^2_{L^2(|\boldsymbol{x}|<a)}$.

(ii) To establish (4.2), one writes

$$\begin{aligned}|\nabla\psi|^2_{L^2(|\boldsymbol{x}|>a)} &= \mathcal{H} - |\nabla\psi|^2_{L^2(|\boldsymbol{x}|<a)} + \frac{1}{2}|\psi|^4_{L^4} - \int V|\psi|^2\,\mathrm{d}\boldsymbol{x} \leq \mathcal{H} + \frac{1}{2}|\psi|^4_{L^4(|\boldsymbol{x}|<a)} + \frac{1}{2}|\psi|^4_{L^4(|\boldsymbol{x}|>a)}\\ &\leq \mathcal{H} + C|\rho_a\psi|^4_{L^4} + \frac{\mathcal{E}}{2}|\psi|^2_{L^\infty(|\boldsymbol{x}|>a)} \leq C + C|\rho_a\psi|^4_{L^4} + C|\nabla\psi|_{L^2(|\boldsymbol{x}|>a)}\\ &\leq C(1 + |\nabla(\rho_a\psi)|^2_{L^2}) + \frac{1}{2}|\nabla\psi|^2_{L^2(|\boldsymbol{x}|>a)},\end{aligned} \tag{4.13}$$

where C holds for various constants and where the inequality $|v|_{L^s(|\boldsymbol{x}|<a)} \leq C|\rho_a v|_{L^s}$ was used. It follows that:

$$\limsup_{t\to T} \frac{|\nabla\psi|^2_{L^2(|\boldsymbol{x}|>a)}}{|\nabla(\rho_a\psi)|^2_{L^2}} = \text{const.} \tag{4.14}$$

From the inequalities

$$|\psi|^4_{L^4(|\boldsymbol{x}|>a)} \leq \mathcal{E}|\psi|^2_{L^\infty(|\boldsymbol{x}|>a)} \leq C|\nabla\psi|_{L^2(|\boldsymbol{x}|>a)}, \tag{4.15}$$

Eq. (4.2) follows.

To establish Eq. (4.3), one starts from

$$\mathcal{H} = \int_{|\boldsymbol{x}|<a} |\nabla\psi|^2\,\mathrm{d}\boldsymbol{x} + \int_{|\boldsymbol{x}|>a} |\nabla\psi|^2\,\mathrm{d}\boldsymbol{x} - \frac{1}{2}\int_{|\boldsymbol{x}|<a} |\psi|^4\,\mathrm{d}\boldsymbol{x} - \frac{1}{2}\int_{|\boldsymbol{x}|>a} |\psi|^4\,\mathrm{d}\boldsymbol{x} + \int V(\boldsymbol{x})|\psi|^2\,\mathrm{d}\boldsymbol{x}. \tag{4.16}$$

Dividing by $\int_{|\boldsymbol{x}|<a} |\nabla\psi|^2\,\mathrm{d}\boldsymbol{x}$ and taking the limit $t \to T$, one gets that

$$\lim_{t\to T}\left(\frac{\int_{|\boldsymbol{x}|<a} |\psi|^4\,\mathrm{d}\boldsymbol{x}}{\int_{|\boldsymbol{x}|<a} |\nabla\psi|^2\,\mathrm{d}\boldsymbol{x}}\right) = \text{const.} \neq 0. \tag{4.17}$$

As a consequence,

$$\int_{|\boldsymbol{x}|<a} |\psi|^4\,\mathrm{d}\boldsymbol{x} \to \infty, \tag{4.18}$$

and so does $|\psi|_{L^\infty(|\boldsymbol{x}|<a)}$. □

4.2. Numerical results

The above proposition establishes that axisymmetric collapsing solutions are necessarily singular at the origin but does not exclude that a ring singularity also forms (see Eq. (4.14)), in spite of estimate (4.2) that provides an upper

bound for the behavior of the L^4-norm restricted to a region not including the origin. Nevertheless, in the context of the usual NLS equation at critical dimension, one expects that blowup can only take place at a finite number of isolated points. Although the existing rigorous analysis [19] does not totally exclude the possibility of a ring singularity, it makes it highly implausible. We expect this situation to also hold in the presence of a potential, as the latter becomes negligible near collapse. More insight into the question of the existence and nature of singularities can be gained by numerical simulations, that in the axisymmetric context can be carried out in details.

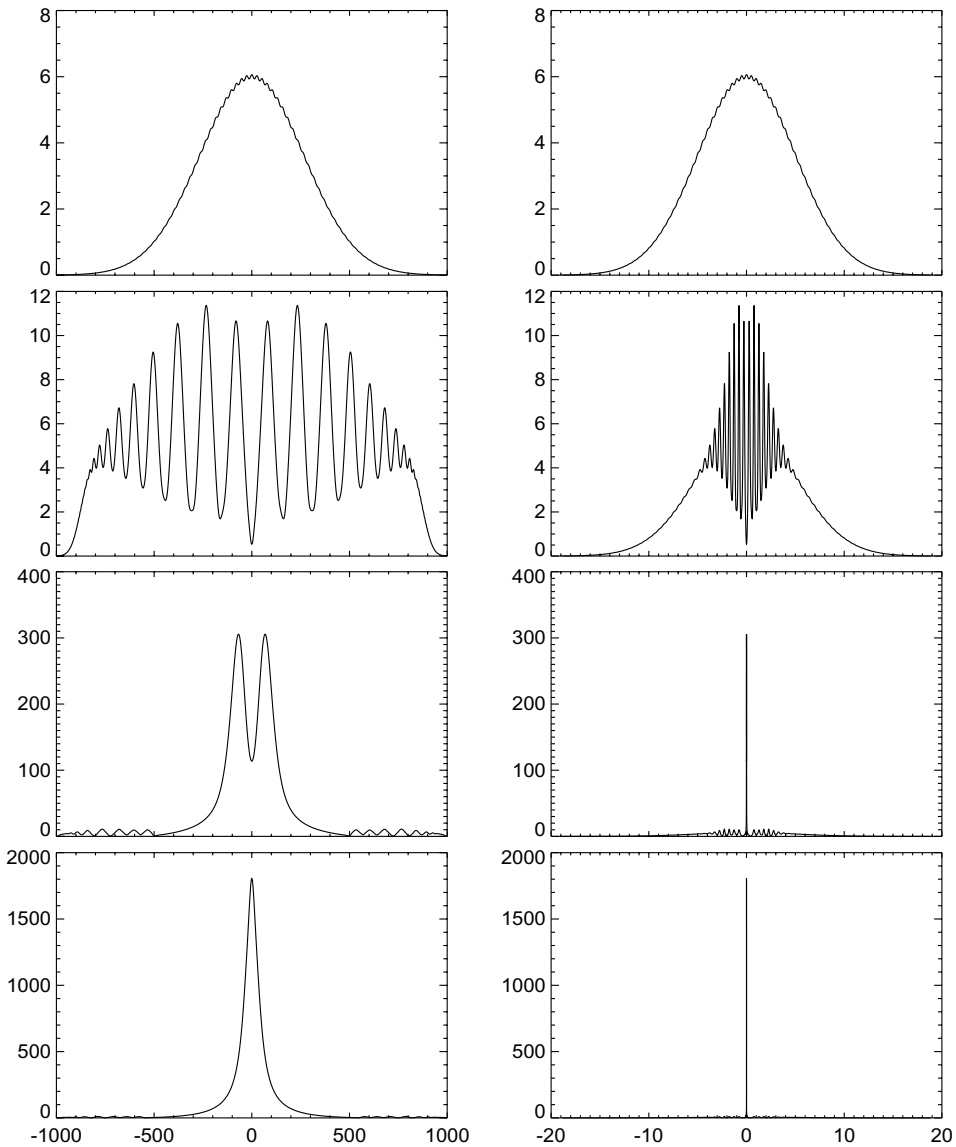

Fig. 12. Adaptive mesh integration of the NLS equation (3.1) for an axisymmetric Alfvén beam with an initial amplitude $B_0 = 6\,\mathrm{e}^{-0.02|\boldsymbol{x}|^2}(1 + 0.01\cos(4\pi|\boldsymbol{x}|))$. The magnetic field intensity $|B|^2$ along a diameter is displayed. Left column: profile in the computational space; right column: corresponding profile in physical space. From top to bottom, the panels refer to times $T = 0$, 0.121, 0.1633 and 0.1634.

The simulations presented in Section 3.3 suggest that an Alfvén-wave beam with an initial profile $B_0 = A\,\mathrm{e}^{-(1/\delta^2)|\boldsymbol{x}|^2}$ (here $|\boldsymbol{x}|^2 = y^2 + z^2$) with a maximum amplitude $A = 6$ and a width $\delta = 1$ develops, under the effect of the repulsing potential, an intensity ring that moves outwards and eventually disperses. A similar dynamics is observed when the width of the beam is decreased, leading to a broader ring that spreads even faster. In contrast, when keeping the same maximal amplitude, the width of the beam is enlarged (or equivalently keeping the width, the amplitude is increased), a modulational instability can develop near the maximum, with a wavelength $\lambda = (2\pi/A)\sqrt{(\alpha/g)}$ in the units of Eq. (3.1). This estimate assumes that the beam width δ is sufficiently large compared to λ so that the wave packet can be locally viewed as a plane wave. The presence of the potential affects neither the instability wavelength nor its growth rate, compared to the usual NLS regime. With the values of k and β we used in the present simulation, one has $\lambda \approx 3.27/A$. In such a regime where $\delta \gg \lambda$, the dynamics will be similar to that of a plane wave where modulational instability induces wave collapse. We checked numerically that this effect indeed occurs as soon as $\delta/\lambda \approx 7$. This regime is illustrated in Fig. 12 that was performed using a one-dimensional version of the mesh refinement algorithm mentioned in the previous section and described in Appendix A. This simulation corresponds to an initial condition of the form $B_0 = 6\,\mathrm{e}^{-0.02|\boldsymbol{x}|^2}(1+0.01\cos(4\pi|\boldsymbol{x}|))$, where the cosine perturbation has a wavelength comparable to that characteristic of the modulational instability. One indeed observes the formation of several concentric rings and eventually a collapse at the center. As expected, the wavelength of the instability is close to 0.5. Note that in the presence of the potential, the minimum L^2 norm of the solution for collapse strongly exceeds the critical value for the usual two-dimensional NLS equation.

A similar dynamics is obtained when the same Gaussian profile $B_0 = 6\,\mathrm{e}^{-0.02|\boldsymbol{x}|^2}$ is perturbed by a random noise with a 10^{-4} maximal amplitude. The details of the dynamics are however different. Rings form one at a time,

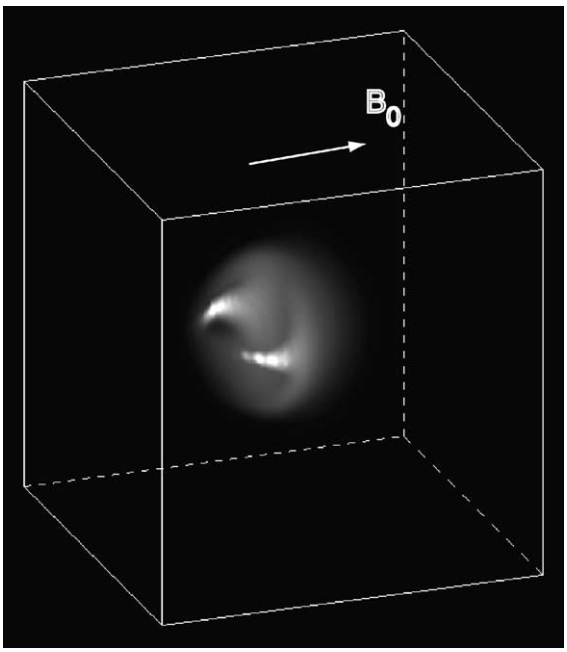

Fig. 13. Perspective volume-rendering visualization of the transverse magnetic field intensity obtained at $T = 0.3$ by a simulation of amplitude equations (2.11)–(2.14), starting from an Alfvén-wave packet of amplitude $B_0 = 6\,\mathrm{e}^{-[(1/25)(x-5\pi)^2+2.5(y-\pi)^2+(z-\pi)^2]}$. The longitudinal extension of the box is in fact 5 times bigger than the transverse ones, making the intense magnetic structures more elongated in this direction than they appear.

move towards the origin and stay there. After several such events, the amplitude at the origin starts increasing and a collapse eventually takes place.

As the width of the initial profile is sufficiently reduced, for example by taking $B_0 = 6\,\mathrm{e}^{-0.3|\boldsymbol{x}|^2}$, several concentric rings are still formed and a maximal amplitude equal to about twice the initial one is reached, but these structures eventually move outwards while the maximum amplitude decreases.

The critical width for beam collapse is delicate to estimate accurately. For example for initial condition $B_0 = 6\,\mathrm{e}^{-0.05|\boldsymbol{x}|^2}$, peaks reach amplitudes of a few thousands when they are still at a small but finite distance (of order 10^{-3}) from the axis, indicating that, in spite of the large amplitude, the system did not yet reach the asymptotic regime for collapse.

5. Alfvén-wave packets

We consider in this section the dynamics of a wave packet with a finite extension in all three directions. Such simulations are sensitive to the presence of unstable oblique modes. Nevertheless, in contrast with the case of an infinite Alfvén-wave train, the oblique instabilities do not prevent the integration of the envelope equations, at least when the aspect ratio of the computational box permits a refined description of the quasi-transverse Fourier modes. In this case, the collapse dynamics can dominate the small-scale linear instabilities. This enables one to perform additional comparisons between prediction of the envelope equations and results of direct numerical simulations. It

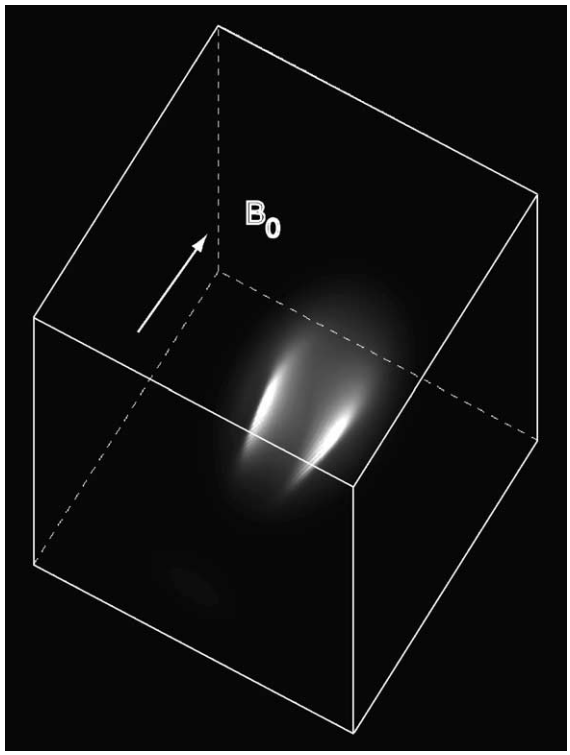

Fig. 14. Perspective volume-rendering visualization of the transverse magnetic field intensity obtained at $t = 130$ by a direct simulation of an Alfvén-wave packet with an initial amplitude $\mathrm{e}^{-(1/288)[(1/25)(x-48\pi)^2+(y-10\pi)^2+2.25(z-10\pi)^2]}$. The longitudinal extension of the box is in fact 4.8 times bigger than the transverse ones, making the intense magnetic structures more elongated in this direction than they appear.

turns out that wave collapse can develop in the case of wave packets that are sufficiently extended in the longitudinal direction.

Two regimes are observed according to the longitudinal extension of the wave packet. In the context of the amplitude equations, one observes that for an initial Alfvén-wave packet of amplitude $B(\boldsymbol{x},0) = 6\,\mathrm{e}^{-[(x-5\pi)^2+2.5(y-\pi)^2+(z-\pi)^2]}$ with zero initial density fluctuations and mean longitudinal fields, a shell forms at early times but dispersion proceeds and collapse is prevented. This simulations was performed in a box of extension $10\pi \times 2\pi \times 2\pi$ using a resolution of 128^3 collocation points. In contrast, with a longer wave packet defined by $B_0 = 6\,\mathrm{e}^{-[(1/25)(x-5\pi)^2+2.5(y-\pi)^2+(z-\pi)^2]}$ a three-dimensional wave collapse is observed in the same computational conditions, with a maximal transverse magnetic field intensity of 134 at time $T = 0.3$, before the simulation breaks down. The intense magnetic structures that are formed are displayed in Fig. 13. Note that the longitudinal extension of the computational box is actually 5 times bigger than the transverse ones. The displayed structure should thus be stretched accordingly, and are thus more elongated than suggested by the picture.

A similar collapse is observed in the direct numerical simulation of an Alfvén wave with an initial amplitude $0.1\,\mathrm{e}^{-(1/288)[(1/25)(x-48\pi)^2+(y-10\pi)^2+2.25(z-10\pi)^2]}$, in a computational box of size $96\pi \times 20\pi \times 20\pi$. A resolution $1024 \times 128 \times 256$ is used. Even such a large resolution is not sufficient to obtain very intense magnetic structures, and the maximal transverse magnetic intensity obtained is 0.045 before the simulation breaks down. The resulting structure is displayed in Fig. 14. In this case also, a scaling by a factor 4.8 has to be applied in the longitudinal direction to obtain the real picture.

In both computations, the high intensity regions appear to be fragments of thin filaments that could result from the transverse collapse of modulated elongated structures. Furthermore, even if the blowup eventually takes place at an isolated point, the dynamics probably does not consist in an isotropic three-dimensional collapse.

6. Conclusion

Dispersive Alfvén waves provide an interesting framework to test the predictive character of the envelope formalism beyond its strict domain of validity. For this purpose, comparisons with direct numerical simulations of the Hall-MHD equations were performed for various kinds of initial conditions. A main observation concerns the formation of intense magnetic filaments, an effect associated with the phenomenon of wave collapse predicted by the amplitude equations.

Alfvén-wave beams with a homogeneous intensity along the propagation axis show a peculiar dynamics accurately described by an NLS equation with an additional potential proportional to the initial amplitude of the wave. Their evolution depends on the width of the beam and also on the presence of azimuthal perturbations. At early time, the amplitude on the beam axis decreases. This mechanism is coupled to the development of a modulational instability if the beam is wide enough, leading to a concentration of its energy on co-axial cylindrical surfaces. During this process, an initial anisotropy increases and wave collapse can rapidly develop on off-center filaments. When axisymmetry is enforced, collapse has to take place on the beam axis and, for a given width, the critical amplitude for collapse is significantly larger than in the non-axisymmetric case. Equivalently, for a fixed amplitude, collapse requires that the beam be sufficiently large. The above dynamics is a consequence of the considered class of initial conditions, where only transverse velocity and magnetic field components are perturbed. This situation differs from the regime studied in [3,21], where only the dynamics near collapse was considered, by taking for the initial longitudinal velocity $\bar{u}_x(0) = |B_0|^2$ instead of $\bar{u}_x(0) = 0$. In that case the system obeys the standard NLS equation.

When the beam has also a finite extension in the longitudinal direction, similar three-dimensional anisotropic collapsing structures are observed in direct simulations of the Hall-MHD equations and by integration of the envelope equations. For such a finite-time collapse, a minimum length of the wave packet is also necessary.

The phenomenon of Alfvén-wave collapse addressed in this paper provides an efficient mechanism for small-scale formation, resulting from the instability of a small-amplitude wave. Such an effect is expected to heat the plasma. An important question for astrophysical application concerns its persistence in the more general context of Alfvén-wave turbulence. Preliminary results provided by the CLUSTER satellites tend to indicate the presence of intermittent structures in the form of current tubes whose diameter is comparable to ion Larmor radius in the earth magneto-sheath, where dispersive Alfvén waves and turbulence are conspicuous features [22].

Furthermore, the description provided by the Hall-MHD equation may be insufficient in the case of a collisionless plasma when kinetic effects such as the Landau damping may be relevant. Their influence on the filamentation phenomenon remains an open problem in the general case but is amenable to a systematic analysis in the limit of long Alfvén waves [23–25].

Acknowledgements

Direct simulations were performed at the Institut du Développement et des Ressources en Informatique Scientifique. Support from France–Hong Kong PROCORE collaboration program, CNRS "Programme National Soleil Terre", NSERC Operating grant OGP0046179 and INTAS grant 2000-292 is also acknowledged. The work of D.S. Wang and X.P. Wang is also supported in part by RGC Competitive Earmarked Research grant HKUST 6176/99P and HKUST 6143/01P.

Appendix A. Adaptive method based on an IGR

The adaptive method used in this paper follows the iterative grid redistribution (IGR) algorithm introduced in [14], based on a variational approach. Grid redistribution is needed if the integrated solution presents quasi-singular features (large amplitudes, strong derivatives) because, in this case, a fixed Cartesian mesh cannot be sufficient to achieve the computation with the required accuracy. The mesh points can then be redistributed in an adaptive way, to make the evolving solution better behaved. This is accomplished by a coordinate transformation, which is recalculated and applied whenever it is needed, according to some criterion based on the actual solution. More explicitly, remeshing is applied whenever either the truncation error or some combination of the solution of its derivatives gets larger than a chosen threshold. In the following we briefly describe the remeshing algorithm.

Let $\boldsymbol{x}$ and $\boldsymbol{\xi}$ denote the physical and computational coordinates defined in domains $\Omega \subset \mathbf{R}^d$ and $\Omega' \subset \mathbf{R}^d$, respectively. They correspond by a one-to-one coordinate transformation denoted by $\boldsymbol{x} = \boldsymbol{x}(\boldsymbol{\xi})$. To establish this transformation, a variational method is used by minimizing some functional which, in the existing approaches, is usually expressed in the form

$$E(\boldsymbol{\xi}) = \int_{\Omega} \sum_{i,j,\alpha,\beta} g^{ij} \frac{\partial \xi^{\alpha}}{\partial x^{i}} \frac{\partial \xi^{\beta}}{\partial x^{j}} \, \mathrm{d}\boldsymbol{x}, \tag{A.1}$$

where $G = (g_{ij})$, $G^{-1} = (g^{ij})$ are symmetric positive definite matrices which are functionals of the integrated solutions, here denoted by $u(\boldsymbol{x})$. The g_{ij} control the coordinate transformation by monitoring the behavior of $u(\boldsymbol{x})$ and are called monitor functions. The transformation $\boldsymbol{x} = \boldsymbol{x}(\boldsymbol{\xi})$ and the new mesh are determined from the Euler–Lagrange equation

$$\nabla \cdot (G^{-1} \nabla \boldsymbol{\xi}) = 0, \tag{A.2}$$

where the gradients are taken with respect to the $\boldsymbol{x}$ variable. More terms can be added to the functional (A.1) to control other properties of the mesh, such as its orthogonality or the alignment of the mesh lines with a prescribed vector field [20].

The choice of the monitor functions g_{ij}, which must take into account the variation of the solution and of its derivatives, is problem-dependent, but in most cases good results can be obtained by using simple functions of the solution and of its derivatives.

The mesh transformation used in this paper is based on an IGR procedure defined as follows. At stage k of this iteration, the $\boldsymbol{x}^{k+1}$-mesh is constructed by the transformation $(\boldsymbol{x}^k, u^k(\boldsymbol{x}^k)) \to (\boldsymbol{x}^{k+1}, u^{k+1}(\boldsymbol{x}^{k+1}))$, where $u^{k+1}(\boldsymbol{x}^{k+1}) = u^k(\boldsymbol{x}^k(\boldsymbol{x}^{k+1}))$ with $\boldsymbol{x}^{k+1}(\boldsymbol{x}^k)$ defined from $u^k(\boldsymbol{x}^k)$ according to (A.2), the monitor matrix G^k being constructed using $u^k(\boldsymbol{x})$. This procedure is repeated until a suitable mesh is obtained.

The incorporation of the above algorithm into a static adaptive method for solutions of partial differential equations (PDEs) is then straightforward. In particular, an initial mesh distribution is determined by the IGR in such a way that a prescribed criterion involving the initial condition is met. We then solve the PDE in the computational variable $\boldsymbol{\xi}$ until some time t^* when the solution $u(\boldsymbol{\xi}, t^*)$ cannot satisfy anymore this criterion. Then the computation stops, a new mesh distribution $\boldsymbol{x}(\boldsymbol{\xi})$ is generated, the solution is calculated on the new grid points by cubic interpolation and the integration of the equation can proceed.

In the coordinate system $\boldsymbol{\xi} = (\eta, \zeta)$, the two-dimensional NLS equation with additional linear potential (3.1) discussed in Section 3.3 becomes

$$B_t - \mathrm{i}(\alpha \mathcal{D}B - C_1|B|^2 B + C_2 B) = 0, \tag{A.3}$$

where (Greek subscripts denoting derivatives)

$$\mathcal{D}B = \frac{1}{J}\left\{ \frac{\partial}{\partial \eta}\left(\frac{b_{22}B_\eta - b_{12}B_\zeta}{J} \right) + \frac{\partial}{\partial \zeta}\left(\frac{b_{11}B_\zeta - b_{12}B_\eta}{J} \right) \right\}, \tag{A.4}$$

$$b_{11} = x_\eta^2 + y_\eta^2, \qquad b_{12} = x_\eta x_\zeta + y_\eta y_\zeta, \qquad b_{22} = x_\zeta^2 + y_\zeta^2 \tag{A.5}$$

with $\boldsymbol{x} = (y, z)$. Here J is the Jacobian of the coordinate transformation. We also use $C_1 = k((1/v_\mathrm{g}) - (v_\mathrm{g}k^4/4(\beta+1)\omega^4))$ and $C_2 = (k/v_\mathrm{g})|B_0|^2$. In the grid redistribution, the monitor matrix is taken to be diagonal with

$$g_{1,1}(\eta, \zeta) = 1 + 0.1\frac{|B(\eta, \zeta)|}{|B(\eta, \zeta)|_{\max}} + \frac{|B_\eta(\eta, \zeta)|}{|B_\eta(\eta, \zeta)|_{\max}}, \tag{A.6}$$

$$g_{2,2}(\eta, \zeta) = 1 + 0.1\frac{|B(\eta, \zeta)|}{|B(\eta, \zeta)|_{\max}} + \frac{|B_\zeta(\eta, \zeta)|}{|B_\zeta(\eta, \zeta)|_{\max}}. \tag{A.7}$$

A finite-difference space discretization is used to solve this system. The remeshing criterion is set so that the maximum of the gradient is smaller than a given value TOL = 12.5. The transformed system is solved on Ω' with $[201 \times 201]$ grid points. A second order Runge–Kutta method is used for the time integration. In the case of the initial conditions $B_0(x, y) = 6\,\mathrm{e}^{-[1.3(x-\pi)^2+(y-\pi)^2]}$, about 27 remeshing steps are performed before the computation reaches the time $\tau = 0.32254$ when the maximum value of the wave intensity $|B|^2$ is 1.4923×10^4 and the minimum mesh size 1.2×10^{-3}.

References

[1] C. Sulem, P.L. Sulem, The nonlinear Schrödinger equation: self-focusing and wave collapse, Applied Mathematical Sciences, vol. 139, Springer, Berlin, 1999.
[2] J.X. Xin, Physica D 135 (2000) 345.

[3] S. Champeaux, T. Passot, P.L. Sulem, J. Plasma Phys. 58 (1997) 665.
[4] P.K. Shukla, L. Stenflo, Astrophys. Space Sci. 155 (1989) 145.
[5] D. Laveder, T. Passot, P.L. Sulem, Phys. Plasmas 9 (2002) 293.
[6] V.C.A. Ferraro, Proc. R. Soc. London Ser. A 233 (1955) 310.
[7] B.T. Tsurutani, E.J. Smith, D.E. Jones, J. Geophys. Res. 88 (1983) 5645.
[8] M.L. Goldstein, C.W. Smith, W.H. Matthaeus, J. Geophys. Res. 88 (1983) 9989.
[9] S. Spangler, S. Fuselier, A. Fey, G. Anderson, J. Geophys. Res. 93 (1988) 845.
[10] D. Laveder, T. Passot, P.L. Sulem, Phys. Plasmas 9 (2002) 305.
[11] V.E. Zakharov, Sov. Phys. JETP 35 (1972) 908.
[12] M.J. Landman, G.C. Papanicolau, C. Sulem, P.L. Sulem, X.P. Wang, Phys. Rev. A 46 (1992) 7869.
[13] C. Canuto, Y. Hussaini, A. Quarteroni, T.A. Zang, Spectral Methods in Fluid Dynamics, Springer, Berlin, 1988.
[14] W. Ren, X.P. Wang, J. Comput. Phys. 159 (2000) 246.
[15] A.J. Leggett, Rev. Mod. Phys. 73 (2001) 307.
[16] H.A. Rose, M.I. Weinstein, Physica D 30 (1988) 207.
[17] F. Merle, Y. Tsutsumi, J. Diff. Eqs. 84 (1990) 205.
[18] W. Strauss, Commun. Math. Phys. 55 (1997) 149.
[19] H. Nawa, Commun. Pure Appl. Math. 52 (1999) 193.
[20] J. Brackbill, J. Saltzman, J. Comput. Phys. 46 (1982) 342.
[21] T. Passot, C. Sulem, P.L. Sulem, Physica D 94 (1996) 168.
[22] O. Alexandrova, A. Mangeney, M. Maksimovic, C. Lacombe, N. Cornilleau-Wehrlin, E.A. Lucek, P.M.E. Dècrèau, J.-M. Bosqued, P. Travnicek, A.N. Fazakerley, Cluster observations of finite amplitude Alfvén waves and small scale magnetic filaments downstream of a quasi-perpendicular shock, J. Geophys. Res., to appear.
[23] T. Passot, P.L. Sulem, A long-wave model for Alfvén wave trains in a collisionless plasma: I. Kinetic theory, Phys. Plasmas, in press.
[24] T. Passot, P.L. Sulem, A long-wave model for Alfvén wave trains in a collisionless plasma: II. A Landau-fluid approach, Phys. Plasmas, in press.
[25] T. Passot, P.L. Sulem, Filamentation instability of long Alfvén waves in warm collisionless plasmas, submitted to Phys. Plasmas.